This paper was published in IET Electric Power Applications, 2009, doi 10.1049/iet-epa.2009.0217, and is available at:

http://ieeexplore.ieee.org/stamp/stamp.jsp?tp=&arnumber=5710089

A.A. Abd Hafez, R. Todd, A.J. Forsyth, A.M. Cross, "Direct current ripple compensation for multi-phase fault-tolerant machines," *IET Electric Power Applications*, vol. 5, no. 1, pp. 28-36, January 2011, doi: 10.1049/iet-epa.2009.0217

DC Current Ripple Compensation for Multi-Phase Fault-Tolerant Machines

A.A. Abd Hafez, R. Todd, A.J. Forsyth, A.M. Cross
School of Electrical & Electronic Engineering, The University of Manchester, UK.

Abstract **-** A second-harmonic DC current ripple compensation technique is presented for a multi-phase, fault-tolerant, permanent magnet machine. The analysis has been undertaken in a general manner for any pair of phases in operation with the remaining phases inactive. The compensation technique determines the required AC currents in the machine to eliminate the second-harmonic DC-link current, whilst at the same time minimising the total rms current in the windings. An additional benefit of the compensation technique is a reduction in the magnitude of the electromagnetic torque ripple. Practical results are included from a 70kW, five-phase generator system to validate the analysis and illustrate the performance of the compensation technique.

Index Terms **-** Multi-phase fault-tolerant permanent magnet machines, second-harmonic DC ripple current compensation techniques

1 Nomenclature

α	Phase separation
$\delta_{1,2}$	Angle of $v_{s1,2}$ with respect to $e_{1,2}$
$\theta_{1,2}$	Angle of $i_{s1,2}$ with respect to $e_{1,2}$
ω_e	Electrical angular frequency
ω_m	Mechanical angular velocity
C_{DC}	DC-link capacitor
$e_{1,2}$	Back emfs
$E_{1,2}$	Magnitude of back emfs = $\|e_{1,2}\|$
i_C	DC-link capacitor current
$i_{C(2)}$	Second-harmonic component of i_C
$I_{C(2)}$	Magnitude of second-harmonic current = $\|i_{C(2)}\|$
I_m	$= E/(2X_s)$
$i_{o1,2}$	DC current per phase
$i_{s1,2}$	Stator currents
$I_{s1,2}$	Magnitude of stator currents = $\|i_{s1,2}\|$
L_s	Stator inductance per phase

$m_{1,2}$	Modulation index
P	Total active power of $e_{1,2}$
Q	Total reactive power of $e_{1,2}$
Q_{opt}	Optimal reactive power
R_s	Stator resistance per phase
RE	Normalised residual error
S	Total complex power of $e_{1,2}$
T_e	Electromagnetic torque
V_{DC}	DC-link voltage
$v_{s1,2}$	Converter PWM voltage
$v_{s1,2(1)}$	Fundamental component of $v_{s1,2}$
X_s	Stator reactance per phase

2 Introduction

Multi-phase, fault-tolerant permanent magnet machines are under consideration for a range of high reliability aerospace applications such as electric actuation, fuel pumping and engine-embedded power generation. To provide fault tolerance these machines are designed with a high phase count, such as five [1], for redundancy, a high per-phase impedance, often 1p.u. [2] to limit the fault current, and with mechanical, thermal and electrical isolation between the phases [3]. These features enable the machine to operate with a reduced number of active phases when the other phases are in either a short or open circuit fault condition. The fault-tolerance of the system is maintained in the power electronic interface between the variable amplitude/frequency phase voltages and the common DC bus by the use of separate PWM converters [3, 4] and independent controllers [5]. Five or sometimes six-phase systems [3] are considered to offer the most cost-effective compromise between redundancy and complexity for fault-tolerant aerospace applications.

Research in this area has considered the design options for the machine itself, and the behaviour of the machine under various fault-conditions including shorted turns or windings [6, 7]. Fault-tolerant configurations for the power electronic interface have also been described [8, 9] along with fault detection and fault accommodation techniques [2, 10]. Under many fault conditions, with a reduced number of active phases, the machine becomes unbalanced, resulting in a large torque ripple and a significant low frequency ripple current (usually a second-harmonic) in the DC-link. Several authors [11, 12] have proposed methods to eliminate the

torque ripple under faulted conditions, which involve appropriate adjustment of the AC currents in the remaining healthy phases. However these techniques do not normally result in smooth DC-link power due to the energy stored in the magnetic field of the machine, which is substantial in a fault-tolerant machine. Low frequency DC-link ripple current is a serious concern, especially in aerospace applications, since a much larger capacitor bank would be required, creating a significant weight penalty, especially if high-reliability, non-electrolytic components are used.

This paper provides a detailed examination of the DC-link current in a fault-tolerant generator when only two-phases are active. This represents the most severely unbalanced condition under which it is possible to compensate for the DC-link ripple current using the available active phases. The two-phase case is also relatively straight-forward to analyse, providing valuable insight into the system operation. Analytical expressions are determined for the DC-side second-harmonic current without compensation, which are then used to determine the AC-side conditions that are necessary to eliminate the DC ripple. The optimal reactive power is determined to minimise the rms current as this is likely to result in minimum losses. Steady-state test-rig data from a five-phase generator is used to validate the performance of the compensation technique. Although this work is based on a generator, the analysis and techniques are equally applicable to a fault-tolerant motor drive with a common DC-link.

3 Analysis of Generic Two-Phase System

The simplified equivalent circuit in Fig. 1 shows two-phases of a multi-phase, fault-tolerant, machine system operating from a common DC-link. The phase windings are electrically isolated, and separate, single-phase PWM converters interface the windings to the DC-link. Under normal, balanced operating conditions the second-harmonic DC-side currents of the PWM converters will cancel, minimising the ripple current in the DC-link capacitor, but with a reduced number of active phases the ripple cancellation will be incomplete. This is analysed below when

only two-phases of a five-phase system are active. In Fig. 1 the phase separation (in time) between the winding emfs, e_1 and e_2, is α, and $0 \le \alpha \le \pi$. In the case of a five-phase machine with two active windings α takes the values α=72° for adjacent phases or α=144° for non-adjacent phases.

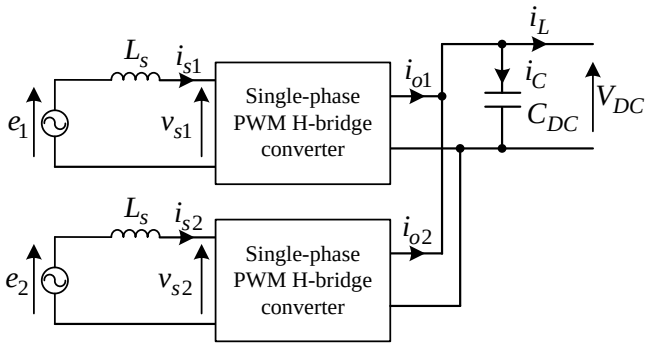

Figure 1. Two-phase system

Each phase winding has an inductance, L_s, but mutual coupling and conduction losses are neglected. Omitting the losses simplifies the analysis, however the experimental results show that the accuracy of the analysis is not seriously compromised. It is assumed that the machine speed is constant over a fundamental period of the input voltages, $v_{s1,2}$, and that the winding currents, $i_{s1,2}$, are sinusoidal with frequency ω_e. The DC-link voltage, V_{DC}, is assumed to have negligible ripple. The phase currents, $i_{s1,2}$, are assumed to have a lagging phase angle, $\theta_{1,2}$, with respect to the machine back emfs, $e_{1,2}$, and the emfs have a phase of $\pm\alpha/2$ with respect to a common reference as shown in the phasor diagram, Fig. 2.

Expressions for the second-harmonic output current from each converter maybe obtained by a power balance calculation. Considering phase 1, the winding back emf and current may be written as $e_1 = E_1 \sin\left(\omega_e t + (\alpha/2)\right)$ and $i_{s1} = I_{s1} \sin\left(\omega_e t + (\alpha/2) - \theta_1\right)$. The fundamental converter input voltage is then:

$$v_{s1(1)} = E_1 \sin\left(\omega_e t + (\alpha/2)\right) - L_s \frac{d}{dt}\left[I_{s1} \sin\left(\omega_e t + (\alpha/2) - \theta_1\right)\right] \tag{1}$$

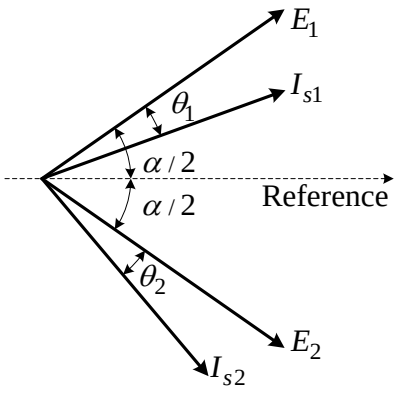

Figure 2. Phasor diagram for two-phase system

Multiplying $v_{s1(1)}$ by i_{s1} to obtain the instantaneous power throughput then dividing by V_{DC} results in the expression for the total DC-side current, i_{o1}. There are two components to i_{o1}, a DC component and a second-harmonic component, $i_{C1(2)}$, which is assumed to flow in the DC-link capacitor. The expression for $i_{C1(2)}$ is:

$$i_{C1(2)} = \frac{-E_1 I_{s1}}{2V_{DC}} \cos\left(2\omega_e t + \alpha - \theta_1\right) - \frac{X_s I_{s1}^2}{2V_{DC}} \sin\left(2\omega_e t + \alpha - 2\theta_1\right) \tag{2}$$

Similarly for phase 2

$$i_{C2(2)} = \frac{-E_2 I_{s2}}{2V_{DC}} \cos\left(2\omega_e t - \alpha - \theta_2\right) - \frac{X_s I_{s2}^2}{2V_{DC}} \sin\left(2\omega_e t - \alpha - 2\theta_2\right) \tag{3}$$

The expressions for the second-harmonic currents (2, 3) have two components, the first is due to the pulsating power flow from the back emfs, $e_{1,2}$, whilst the second is due to the pulsation in stored energy in the magnetic field of the machine. This second term is significant here due to the high winding inductance in a fault-tolerant machine.

Adding $i_{C1(2)}$ and $i_{C2(2)}$, and assuming balanced phases, E_1=E_2=E, results in an expression for the total second-harmonic current in the DC-link capacitor, $i_{C(2)}$. For simplicity the result is expressed as a second-harmonic complex phasor:

$$\mathbf{i_{C(2)}} = \frac{-E}{2V_{DC}} \left(\mathbf{i_{S1}} e^{j\alpha} + \mathbf{i_{S2}} e^{-j\alpha}\right) + \frac{jX_S}{2V_{DC}} \left(\mathbf{i_{S1}^2} e^{j\alpha} + \mathbf{i_{S2}^2} e^{-j\alpha}\right) \tag{4}$$

where $\mathbf{i_{S1}} = I_{S1} e^{-j\theta_1}$ and $\mathbf{i_{S2}} = I_{S2} e^{-j\theta_2}$

Although the derivation has been undertaken for two active phases, the analysis is generic and can be extended to a machine with a higher phase order.

4 Elimination of Second-Harmonic DC-Side Current

To obtain the condition for zero second-harmonic capacitor current, $\mathbf{i_{C(2)}}$, (4), is equated to zero. An additional equation is required to allow an explicit solution for $\mathbf{i_{s1}}$ and $\mathbf{i_{s2}}$ and this may be obtained by considering the total complex power *S* associated with the machine internal emfs:

$$S = \frac{E\mathbf{i}_{\mathbf{s1}}^{*}}{2} + \frac{E\mathbf{i}_{\mathbf{s2}}^{*}}{2} = P + jQ \tag{5}$$

where *P* and *Q* are the total active and reactive powers of the internal machine emf sources and the superscript star denotes the complex conjugate. *P* represents the energy input to the electrical machine and *Q* is the energy stored within the magnetic field of the electrical machine. Rearranging (5) to express $\mathbf{i_{s2}}$ in terms of *S*, and $\mathbf{i_{s1}}$,

$$\mathbf{i_{s2}} = \frac{2S^{*}}{E} - \mathbf{i_{s1}} \tag{6}$$

Substituting (6) into (4) to eliminate $\mathbf{i_{s2}}$, setting $\mathbf{i_{C(2)}}$=0, and then rearranging into a quadratic equation for $\mathbf{i_{s1}}$ results in:

$$a\mathbf{i}_{\mathbf{S1}}^{2} + b\mathbf{i}_{\mathbf{S1}} + c = 0 \tag{7}$$

where $a = jX_s(e^{j\alpha} + e^{-j\alpha})$

$$b = -\left[E(e^{j\alpha} - e^{-j\alpha}) + \frac{j4X_s S^{*} e^{-j\alpha}}{E} \right]$$

$$c = 2S^{*}e^{-j\alpha}\left[\frac{j2X_s S^{*}}{E^{2}} - 1 \right]$$

Solving (7) using the standard formula for a quadratic and simplifying results in:

$$\mathbf{i_{s1}} = I_m\left(j\left(m_s e^{-j\alpha} - 1 \right) \pm sign\sqrt{m_s^2 - 1} \right) \tag{8}$$

Similarly for phase 2

$$\mathbf{i_{s2}} = I_m\left(j\left(m_s e^{j\alpha} - 1\right) \mp sign\sqrt{m_s^2 - 1}\right) \tag{9}$$

where $I_m = \dfrac{E}{2X_s}$, $sign = \begin{cases} +1 \text{ for } 0 < \alpha < \pi/2 \\ -1 \text{ for } \pi/2 < \alpha < \pi \end{cases}$

and $$m_s = \frac{I_m E - jS^*}{I_m E \cos(\alpha)} \tag{10}$$

(8, 9) show that the currents $\mathbf{i_{s1}}$ and $\mathbf{i_{s2}}$ each have two possible solutions.

Set 1 $$\mathbf{i_{s1}} = I_m\left(j\left(m_s e^{-j\alpha} - 1\right) + sign\sqrt{m_s^2 - 1}\right) \quad \mathbf{i_{s2}} = I_m\left(j\left(m_s e^{j\alpha} - 1\right) - sign\sqrt{m_s^2 - 1}\right) \tag{11}$$

Set 2 $$\mathbf{i_{s1}} = I_m\left(j\left(m_s e^{-j\alpha} - 1\right) - sign\sqrt{m_s^2 - 1}\right) \quad \mathbf{i_{s2}} = I_m\left(j\left(m_s e^{j\alpha} - 1\right) + sign\sqrt{m_s^2 - 1}\right) \tag{12}$$

Each set results in zero second-harmonic capacitor current $\mathbf{i_{C(2)}}$=0. However, it is found that Set 1 produces much higher machine currents than Set 2, and so the Set 1 solution is not considered further in this paper. For Set 2, it has been observed that for adjacent phases the $\mathbf{i_{s2}}$ solution has the larger magnitude, whereas for non-adjacent phases active, $\mathbf{i_{s1}}$ is the larger solution.

4.1 Optimal Solution

In solving for the generator currents, (12), the real part of the total complex power *S* in (5) is set by the load requirements and the reactive component may be selected to optimise the system operating conditions, for example to minimise the system losses. Setting the total reactive power, *Q*, to zero would intuitively be the best choice, however it is shown in this section that to minimise the total generator rms current, the optimum value of *Q* is close to, but not equal to zero. The extent to which the optimum condition is degraded by setting *Q*=0 is also qualified.

Standard multi-objective optimisation routines, such as the downhill simplex method, can be used to determine the optimal *Q* that, for example, gives the minimum value of the total generator rms current for a specific load and speed since this is likely to result in minimum overall losses.

However, due to their high computational requirements these routines are unsuitable for use in a real-time controller. Therefore, an approximate analytical result is derived for the optimum Q by assuming that the solution is in the region of Q=0, enabling a Taylor series expansion to be used to simplify the expressions for $\mathbf{i_{s1}}$ and $\mathbf{i_{s2}}$, (12). In particular, the square root in these equations is expanded around m_o, where m_o is the value of m_s, (10), for Q=0.

$$m_o = m_{s(Q=0)} = \frac{I_m E - jP}{I_m E \cos(\alpha)} \tag{13}$$

Only the first two terms of the Taylor series expansion for $\sqrt{m_s^2 - 1}$ around m_o are considered to simplify the analysis. The resulting approximation is,

$$\sqrt{m_s^2 - 1} = \sqrt{m_o^2 - 1} + \frac{m_o (m_s - m_o)}{\sqrt{m_o^2 - 1}} \tag{14}$$

Substituting (14), into (12), the expressions for $\mathbf{i_{s1}}$ and $\mathbf{i_{s2}}$ become,

$$\mathbf{i_{s1}} = I_m \left(j\left(m_s e^{-j\alpha} - 1\right) - sign\left(\sqrt{m_o^2 - 1} + \frac{m_o (m_s - m_o)}{\sqrt{m_o^2 - 1}} \right) \right) \tag{15}$$

$$\mathbf{i_{s2}} = I_m \left(j\left(m_s e^{j\alpha} - 1\right) + sign\left(\sqrt{m_o^2 - 1} + \frac{m_o (m_s - m_o)}{\sqrt{m_o^2 - 1}} \right) \right) \tag{16}$$

The optimal generator reactive power value, Q_{opt}, which results in the minimum sum of squares of the AC currents, $I_{s1}^2 + I_{s2}^2$, can be calculated by solving the following equation, where $I_{s1,2}$ are $|\mathbf{i_{s1,2}}|$.

$$\frac{d}{dQ}\left(I_{s1}^{\,2} + I_{s2}^{\,2} \right) = 0 \tag{17}$$

Substituting (15, 16) into (17), then differentiating, and after considerable manipulation Q_{opt} is found to be:

$$Q_{opt} \approx -E I_m \left[m_s \cos(\alpha) - 1 \right] \tag{18}$$

where $m_s \approx \dfrac{2g_1g_2\cos(\alpha)+\left(m_o+m_o^*\right)-sign\sin(\alpha)(g_1+g_2)}{2g_1g_2+2m_o^*m_o-sign2\sin(\alpha)\left(m_og_1+m_o^*g_2\right)}$,

and $g_1=\sqrt{m_o^{*2}-1}$, $g_2=\sqrt{m_o^2-1}$ and m_o^* is the conjugate of m_o.

Q_{opt}, from (18) has been validated using the downhill simplex optimisation technique [13]. A Matlab program based on the downhill simplex method was written to find the value of the Q_{opt} which results in minimum $I_{s1}^2+I_{s2}^2$ at different operating conditions. The calculation used the values of E and L_s for the 70kW five-phase prototype generator listed in Table 1, and assumed an electrical frequency of 233.33Hz corresponding to a rotational speed of 1000rpm. The correlation between the analytical results, dashed lines in Fig. 3, and the results from the simplex method, solid lines in Fig. 3, are very close for adjacent phases α=72°, Fig. 3.a, but a little less accurate for the non-adjacent phases α=144°, Fig. 3.b, especially at higher speeds, the predicted values from (18) being slightly higher than the results from the simplex method. This was attributed to the much larger values of Q_{opt} when non-adjacent phases are active, breaking the assumption of a solution for Q close to zero. The solution accuracy could be increased by taking more terms in the Taylor series. The approximation used, (18), was considered to be a good compromise between complexity and accuracy.

Speed range	1000-3000rpm
EMF, E	$212V_{pk}$ at 1000rpm
Nominal current, I_s	$116A_{pk}$
Per-phase inductance, L_s	1.3mH
Per-phase resistance, R_s	46mΩ
Phase separation, α	72° adjacent
	144° non-adjacent
Total DC capacitance, C_{DC}	800μF
Switching frequency	10kHz
Pole-pair	14
Dead-time	2μs

Table 1: Parameters of the five-phase 70kW machine

4.2 Solution with Zero Reactive Power

Fig. 3 shows that Q_{opt} is a small fraction of the active power, P, especially at high load levels. Therefore, a simple approximate solution for the optimum values of i_{s1} and i_{s2} may be calculated from (12) by setting S=P, that is Q=0, in (10) in the calculation of m_s. This assumption will simplify further the practical implementation of the second-harmonic DC-side current ripple compensation technique, and it can be justified by considering the normalised residual error, RE:

$$RE = \frac{\left(I_{s1}{}^2 + I_{s2}{}^2\right)_{Q=0} - \left(I_{s1}{}^2 + I_{s2}{}^2\right)_{Q_{opt}}}{\left(I_{s1}{}^2 + I_{s2}{}^2\right)_{Q_{opt}}} \tag{19}$$

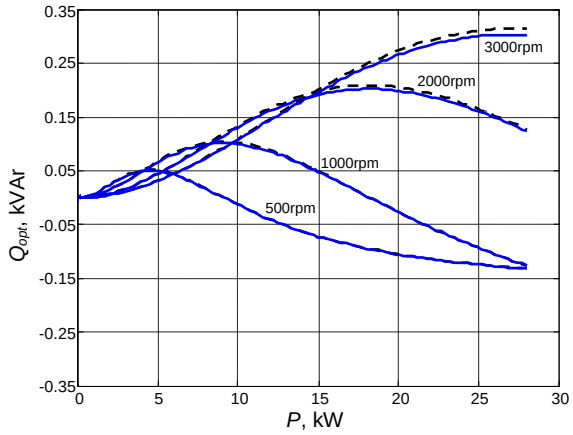

a. adjacent phases (α=72°)

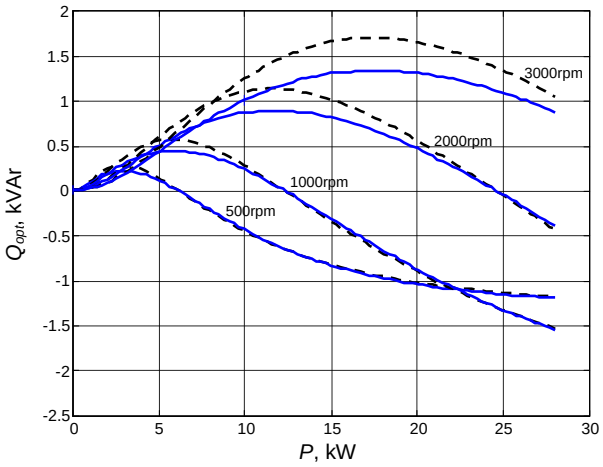

b. non-adjacent phases (α=144°)

Figure 3. Optimal reactive power Q_{opt} from (16) and the downhill simplex versus output power at four speeds

RE calculated using (19) is given in Fig. 4 at different values of generator output power and speed for adjacent (α=72°), Fig. 4.a, and non-adjacent (α=144°), Fig. 4.b, phases.

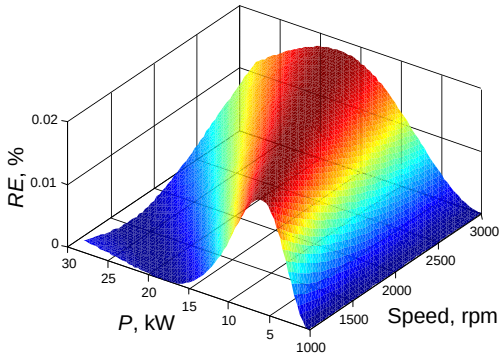

a. adjacent phases (α=72°)

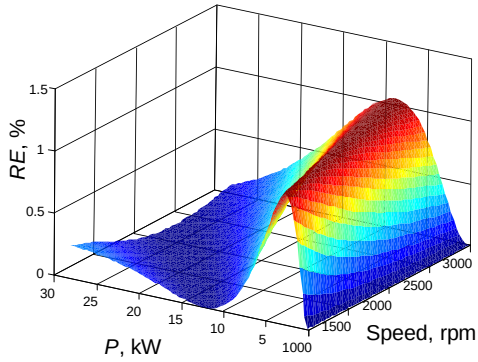

b. non-adjacent phases (α=144°)

Figure 4. Normalised residual error (*RE*) versus generator power and speed

It can be seen in Fig. 4 that the *RE* is negligible, less than 0.02% for adjacent phases, and no more than 1.1% for non-adjacent phases. Therefore the assumption that Q=0 results approximately in minimum system resistive losses is considered to be valid.

5 System Characteristics and Torque Ripple

The impact of the compensation technique on the phase currents, $i_{s1,2}$, is depicted in Figs. 5 and 6 using the parameters of the prototype generator listed in Table 1 across the full power range at the base speed of 1000rpm. The magnitudes, $I_{s1,2}$, and angles, $\theta_{1,2}$, of the phase currents were

calculated using (12) for both adjacent (α=72°) and non-adjacent (α=144°) phases active with zero total reactive power in (10). The plots also show in solid lines I_s and θ of the phase currents assuming identical conditions in both active phases; the phase angle is zero since this minimises the machine currents.

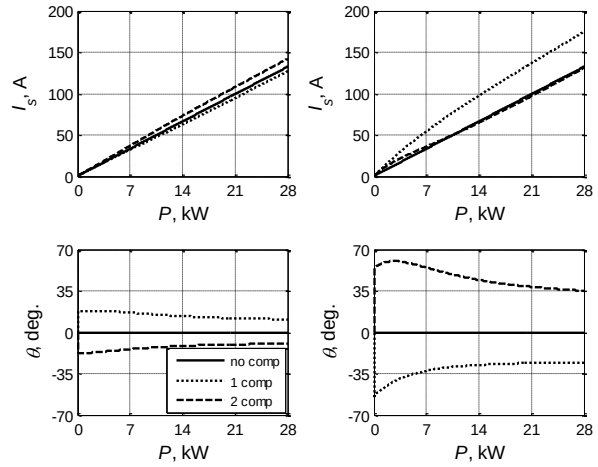

a. adjacent phases (α=72°) b. non-adjacent phases (α=144°)

Figure 5. Phase currents with and without second-harmonic DC capacitor current ripple compensation 1000rpm, 540Vdc

When the system is compensated to eliminate the second-harmonic DC current ripple, I_s and θ become different; with one current becoming larger than the balanced condition value. The difference between the current amplitudes is greater for non-adjacent phases active. The effect of this is to increase one of the phase currents beyond the normal rated level ($116A_{pk}$ for this machine) at higher powers. This may be permissible depending on the thermal design of the machine.

Fig. 6 shows the associated values for the modulation index, m, of the power converters and also the angle, δ, of the fundamental PWM voltage with respect to the phase back emf. In the compensated system m and δ are seen to be increased and decreased from the balanced-system values, which are again shown in solid lines.

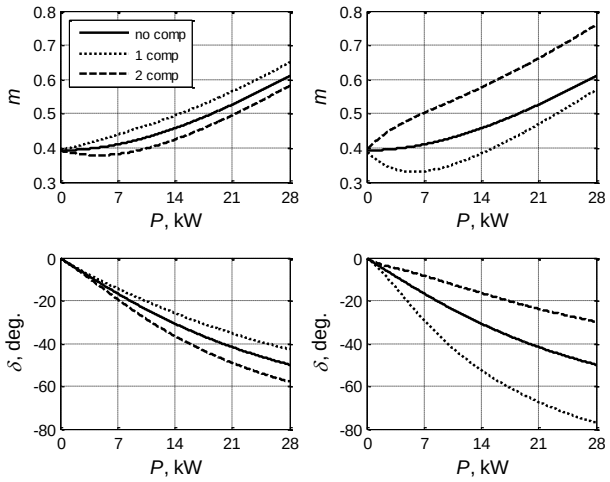

a. adjacent phases (α=72°)

b. non-adjacent phases (α=144°)

Figure 6. Modulation index and voltage angle with and without second-harmonic DC capacitor current ripple compensation

1000rpm, 540Vdc

At higher operating speeds the phase currents will tend to be smaller for a particular output power due to the larger value of the back emfs, consequently the modified phase currents will be more easily accommodated within the normal rating of the machine. However at very high speeds the modulation limit of the power converter will be reached, which may restrict the system's ability to establish the optimum phase currents in the machine windings.

5.1 Torque Ripple

The impact of the second-harmonic DC-side current ripple elimination technique on the torque ripple can be investigated analytically, using (20), which is derived assuming that the mechanical power is equal to the electrical power.

$$T_e = \frac{-E}{2\omega_m}(\mathbf{i_{s1}}e^{j\alpha} + \mathbf{i_{s2}}e^{-j\alpha}) \tag{20}$$

where ω_m is the angular velocity of the rotor.

Fig. 7 shows the predicted torque ripple from (20) for adjacent and non-adjacent phases, α=72° and 144°, with and without the second-harmonic DC-side current ripple compensation. A

significant reduction in the torque ripple occurs up to 50%, at all operating conditions. The residual torque ripple when the second-harmonic DC capacitor current ripple is zero is due to the instantaneous stored energy in the magnetic field of the machine. The high inductance per phase of the machine limits the improvement in torque ripple when the compensation technique is utilised.

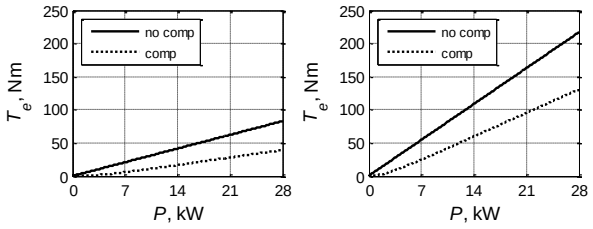

a. adjacent phases (α=72°) b. non-adjacent phases (α=144°)

Figure 7. Calculated torque ripple amplitude with and without second-harmonic DC capacitor current ripple compensation at 1000rpm, 540V

6 Validation

The analytical expressions for the second-harmonic DC-link current with and without the compensation technique have been validated using a combination of steady-state measurements from a 70kW, five-phase prototype generator and a detailed switched simulation. The system parameters are listed in Table 1. The tests were performed by calculating, off-line, the stator current, i_s, for a given speed, load power and DC-link voltage using (12). The corresponding values of the modulation indices, $m_{1,2}$, and the angles of the PWM voltages, $\delta_{1,2}$, were calculated from the equivalent circuit in Fig. 1, then programmed into the control system.

In the switched simulation the machine phases were modelled as sinusoidal back emfs with series inductance and resistance. The PWM converters were modelled with ideal switches which operated at 10kHz with sinusoidal PWM and 2μs dead-time.

Fig. 8.a. shows the results for the second-harmonic capacitor current amplitude, $I_{C(2)}$, when two machine phases are active and no compensation is used. The results are plotted for the cases of adjacent phases active, α=72°, and non-adjacent phases active, α=144°, and for two machine speeds, 500rpm and 1000rpm. The graph shows the theoretical values, the values from simulation and the experimental data; experimental results are only available for adjacent phases.

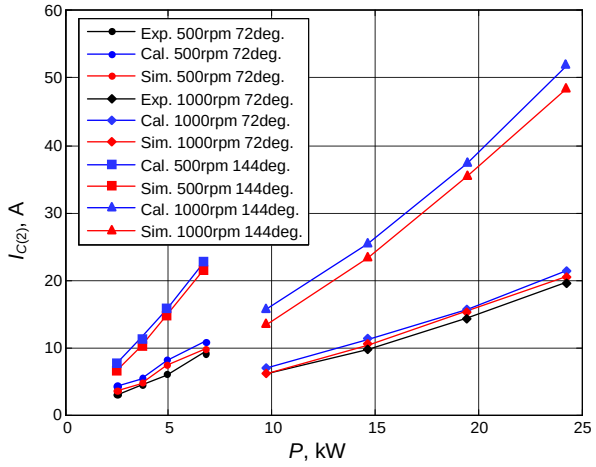

a. without compensation

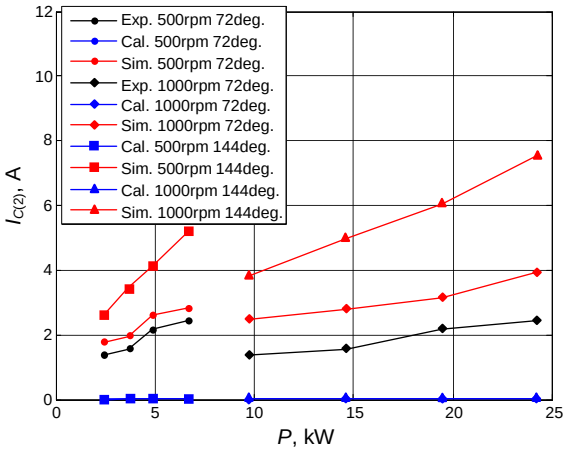

b. with compensation

Figure 8. Capacitor current amplitude, $I_{C(2)}$, versus P at 500rpm and 1000rpm

In all cases there is close correspondence between the predictions, simulation and measurement. The errors are of the order of 10% and the predicted values are always slightly

greater than the experimental data and simulation results. The discrepancies were attributed to the effects of system losses and the leg dead-time in the power converter, which were not included in the theoretical analysis. As expected the second-harmonic current is much greater for the case of non-adjacent phases active.

Fig. 8.b. shows the results for the second-harmonic capacitor current amplitude with the operating conditions calculated using (12) to eliminate, theoretically, the capacitor ripple current. The value of Q was set to zero in (10). The results are again shown for the cases of adjacent, α=72°, and non-adjacent phases, α=144°, at two machine speeds, 500rpm and 1000rpm; for clarity the results are plotted using a finer y-axis scale.

The theoretical values for the second-harmonic current are all zero, however the simulation and experimental results show a significant residual current level. Nevertheless, comparing Fig. 8.b. with the uncompensated case in Fig. 8.a. the capacitor current is substantially reduced, by a factor of between two and five. Larger reductions are obtained at higher current levels. The non-zero values of the capacitor current from the test rig and the simulation were attributed to losses and other second-order effects such as leg dead-time which were not included in the theoretical analysis.

To validate the findings in Section 4.1 for Q_{opt} the values of the converter input currents $\mathbf{i_{s1}}$ and $\mathbf{i_{s2}}$ that eliminate the capacitor second-harmonic current were calculated from (12) for a range of Q levels at 1000rpm with 20Ω and 30Ω loads, corresponding to 14.5kW and 9.7kW respectively, and for adjacent (α=72°) and non-adjacent (α=144°) phases. The modulation indices, $m_{1,2}$, and load angles, $\delta_{1,2}$, of the two-phases were calculated off-line and then programmed into the experimental system and the simulation. The calculated, measured and simulated values of the second-harmonic capacitor current magnitude, $I_{C(2)}$, and the sum of squares of the phase currents, $I_{s1}^2+I_{s2}^2$, are given in Fig. 9. Again, for non-adjacent phases, only simulation and calculated results are shown.

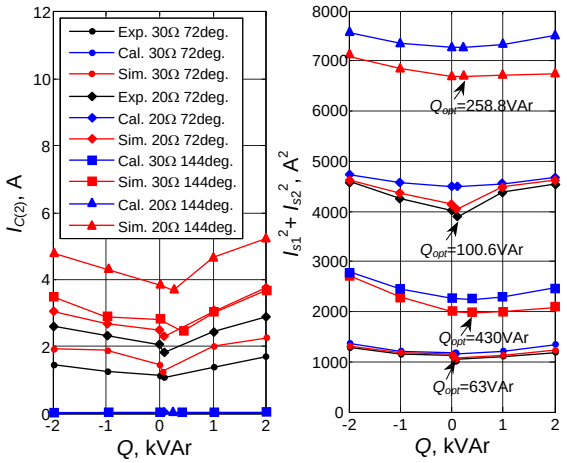

Figure 9. Capacitor current amplitude $I_{C(2)}$ (left) and $I_{s1}^2+I_{s2}^2$ (right) versus Q for 20Ω and 30Ω load at 1000 rpm

The results on the right in Fig. 9 for the sum of squares of the phase currents show a good correspondence between the predicted, measured and simulated values. As may be predicted by the plot in Fig. 5, the sum of squares of the currents is much greater (almost double) for the case of non-adjacent phases than with adjacent phases active assuming the same DC output power.

The results show that the sum of squares of the currents has a fairly flat minimum for values of Q in the region of zero, which confirms the theoretical analysis in sections 4.1 and 4.2. The optimal values of Q calculated from (18) are also marked on the plot. The results confirm that assuming Q=0 is a valid basis for the calculation of the optimal compensation conditions.

The simulation and experimental results for the second-harmonic capacitor current, on the left in Fig. 9, show a small residual current across the range of the values of Q, and the residual current is greater for the case of non-adjacent phases, α=144°. The measured and simulation results show close correspondence. Interestingly the values of residual current tend to be at a minimum for values of Q close to zero, however, this effect is beyond the analysis in this paper, but it is not completely surprising since the total rms machine current is also minimum at this point.

7 Conclusions

The second-harmonic DC-side current ripple has been analysed for a multi-phase, fault-tolerant machine when only two-phases are active. Based on this analysis, expressions have been derived for the machine currents that theoretically result in zero second-harmonic DC-side current ripple. The optimum solution which minimises the sum of squares of the machine current has been found to occur when the total reactive power of the machine back emf sources is close to zero, and furthermore the assumption of zero reactive power has been seen to be a good approximation.

Nevertheless, eliminating the second-harmonic ripple in the DC current has the penalty of increasing the machine currents significantly. The results for the five-phase generator studied here show that with non-adjacent phases active, one of the machine currents is increased by approximately 40% to eliminate the second-harmonic current.

Although the DC-side second-harmonic current is reduced to virtually zero, a significant torque ripple remains, approximately 50% of the value with no compensation, and this was attributed to the energy stored in the magnetic field of the electrical machine.

The theoretical results have been confirmed by experimental measurements and simulations on a five-phase fault-tolerant generator. A small component of second-harmonic current remained in the DC-link capacitor in the experimental and simulation results, around 20% of the original value, and this was attributed to second-order effects such as leg dead-time and system losses which were neglected in the theoretical analysis.

8 Acknowledgements

The authors would like to thank Rolls-Royce plc for funding the experimental system, which forms part of the Intelligent Electrical Power Network Evaluation Facility (IEPNEF) within the Rolls-Royce University Technology Centre in Electrical Systems at the University of

Manchester. IEPNEF has been developed to evaluate ultra-compact and intelligent electrical networks for aerospace, marine and energy applications.

Dr Abd Hafez is grateful to the Egyptian Government for his student scholarship.

9 References

[1] L. Parsa and H. A. Toliyat, "Fault-Tolerant Five-Phase Permanent Magnet Motor Drives," in *Conference Record of the IEEE Industry Applications Conference 39th IAS Annual Meeting*, 2004, vol. 2, pp. 1048-1054.

[2] J. A. Haylock, B. C. Mecrow, A. G. Jack, and D. J. Atkinson, "Operation of a Fault Tolerant PM Drive for an Aerospace Fuel Pump Application," *IEE Proceedings - Electric Power Applications*, 1998, vol. 145, pp. 441-448.

[3] B. C. Mecrow, A. G. Jack, J. A. Haylock, and J. Coles, "Fault-Tolerant Permanent Magnet Machine Drives," *IEE Proceedings - Electric Power Applications*, 1996, vol. 143, pp. 437-442.

[4] T. M. Jahns, "Improved Reliability in Solid-State AC Drives by means of Multiple Independent Phase Drive Units," *IEEE Transactions on Industry Applications*, 1980, vol. IA-16, pp. 321-331.

[5] R. Todd, A. A. Abd Hafez, A. J. Forsyth, and S. A. Long, "Single-Phase Controller Design for a Fault-Tolerant Permanent Magnet Generator," in *IEEE Vehicle Power and Propulsion Conference (VPPC)*, 2008, pp. 1-6.

[6] Z. Sun, J. Wang, D. Howe, and G. Jewell, "Analytical Prediction of the Short-Circuit Current in Fault-Tolerant Permanent-Magnet Machines," *IEEE Transactions on Industrial Electronics*, 2008, vol. 55, pp. 4210-4217.

[7] R. Todd and A. J. Forsyth, "DC-Bus Power Quality for UAV Systems During Generator Fault Conditions," in *IET Power Electronics, Machines and Drives (PEMD)*, Brighton, UK., 2010.

[8] J. W. Bennett, A. G. Jack, B. C. Mecrow, D. J. Atkinson, C. Sewell, and G. Mason, "Fault-Tolerant Control Architecture for an Electrical Actuator," in *IEEE 35th Annual Power Electronics Specialists Conference (PESC)*, 2004, vol. 6, pp. 4371-4377.

[9] L. de Lillo, P. Wheeler, L. Empringham, C. Gerada, and X. Huang, "A Power Converter for Fault Tolerant Machine Development in Aerospace Applications," in *13th Power Electronics and Motion Control Conference (EPE-PEMC)*, 2008, pp. 388-392.

[10] J. Zhu, N. Ertugrul, and W. L. Soong, "Detection and Remediation of Switch Faults on a Fault Tolerant Permanent Magnet Motor Drive with Redundancy," in *2nd IEEE Conference on Industrial Electronics and Applications (ICIEA)*, 2007, pp. 96-101.

[11] J. Wang, K. Atallah, and D. Howe, "Optimal Torque Control of Fault-Tolerant Permanent Magnet Brushless Machines," *IEEE Transactions on Magnetics*, 2003, vol. 39, pp. 2962-2964.

[12] J. Zhu, N. Ertugrul, and W. L. Soong, "Minimum Torque Ripple Current Control Strategy in a Dual Fault Tolerant PM AC Motor Drive," in *IEEE Power Electronics Specialists Conference (PESC)*, 2008, pp. 1542-1547.

[13] C. Blum and A. Roli, *Metaheuristics in Combinatorial Optimization: Overview and Cconceptual Comparison*: Vol. 35: ACM Press New York, NY, USA, 2003.